Journal of Materials Chemistry A

Accepted Manuscript

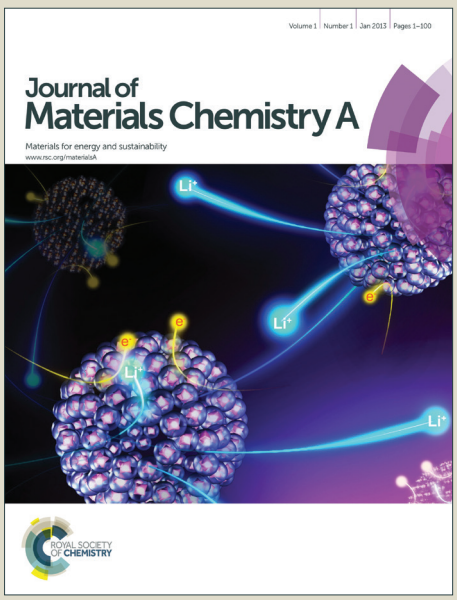

ROYAL SOCIETY OF CHEMISTRY

www.rsc.org/materialsA

Journal Name

RSCPublishing

ARTICLE

Superiority of the bi-phase mixture of tin-based alloy nanocomposite as anode for lithium ion batteries

Cite this: DOI: 10.1039/x0xx00000x

Xue Li[a], Xinyi He[a], Yuefeng Xu[a], Ling Huang[a]*, Juntao Li[b], Shigang Sun[a], Jinbao Zhao[a]

Received 00th January 2012,
Accepted 00th January 2012

DOI: 10.1039/x0xx00000x

www.rsc.org/

The nanostructured mixture of Sn_2Fe and Sn_2Co alloy composite with uniform cubic shape particles has been synthesized by reduction-thermal diffusion alloying reaction. The textural properties of the as-prepared samples were characterized by field-emission scanning electron microscopy, transmission electron microscopy and powder X-ray diffraction. Compared with the Sn_2Fe alloy, the alloy composite exhibits better reversibility and cycle performance. At charge/discharge current density of 50 mA/g, a reversible capacity of 510 mAh/g can be maintained after 50 cycles, and its capacity in the 50 th cycle was retained at ca. 85% of that in the second cycle. When the current density is increased to 1000 mA/g, a reversible capacity of 443 mAh/g can be still obtained. The Ab-initio Simulation results indicated the Sn_2Fe and Sn_2Co have the similar crystal structure, demonstrating the two kinds of alloys can be mixed uniformly by thermal diffusion alloying reaction. The superior electrochemical performance can be attributed to the homogenous-dispersed inactive metallic material (Fe and Co) with nanostructure, which accommodates partly the volume change and also keep the integrity of the active material and matrix, resulting in good cycle performance of the composite electrode.

Introduction:

Lithium-ion batteries as the most suitable power of portable electronic devices bring a lot of convenience to people. On account of the high performance of mobile electronic devices, people have higher expectations for the lithium-ion batteries with energy density. Due to the little room for the development of high capacity cathode materials, the capacity increasing for LIBs in the past five years almost contributes to the improved performance of the anode materials. Therefore, much attention has been focused on the new type anode materials with novel structure prepared by original and facile methods [1-5]. At present, graphite is normally used as an anode material for lithium ion batteries with a relatively low theoretical capacity 372 mAh g^{-1}. Compared with graphite, tin-based material has been regarded as the one of the most potential candidates due to the high theoretical specific capacity (994 mAh g^{-1}). [6-7] However, it is well known that pure tin metal electrode suffers from large volume expansion (about 358%)[8] during the charge–discharge process, leading to mechanical disintegration and very poor cycle life. To solve this problem, Winter et al. has proposed that preparing alloy or composite materials can improve the cycling performance [9]. For the alloy materials, Li_xMSn phase or mixture phase of $Li_{4.4}Sn$ and metal M can form during the alloying–dealloying process. Among of these phases, the inactive phase M offers buffer matrix to relief volume expansion during the charge–discharge process and also plays a role in maintaining the integrity between the particles, the active material and the current collector [10]. These alloys such as Cu_6Sn_5[11], SnNi [12], SnSb [13], SnCoC [14], SnSbM [15], and so forth, have shown a good reversible specific capacities. Amongst tin-based alloys, SnFe alloy gets much attention in recent years with its advantage of good conductivity, low cost, open architecture, high capacity [16]. Zhang et al. demonstrated Sn_2Fe alloy with particle size of 80 nm derived from hydrothermal synthesis could deliver reversible capacity of 500 mAh g^{-1} [17-18]. Chamas et al. studied the electrochemical performance of nanoscale Sn_2Fe particles, they have found the nanoscale material exhibited relatively high capacity, but there was a rapid decay after 40 cycles [19].

In summary, higher capacity can be obtained for SnFe alloy in nanoscale. However, the cycling performance of nanomaterial is still poor as report and there is always a rapid capacity fading after 30 cycles. In this work, cubic bi-phase SnFeCo alloy was fabricated by chemical reduction-thermal diffusion alloying reaction with the particle size of 106 nm in narrow distribution. As anode materials for lithium ion batteries, the alloy composite exhibits better reversibility and cycle performance. Based on density functional theory (DFT),

we have used the Vienna Ab-initio Simulation Package (VASP) to calculate crystal structure parameters of the as-prepared alloy material and explore the electrochemical process of the as-prepared Sn-based composite material. The post-cycling microstructure characterization and XPS spectrum analysis are also carried to investigate the alloy electrodes. And all the data can consistently prove that the bi-phase mixture of tin-based alloy has the superiority for lithium storage compared with the single-phase alloy.

Experimental section

Material preparation

In a typical synthesis of intermetallic SnFeCo nanocrystals, 1.0 g of PVP was dissolved in 50 ml tetraethylene glycol (TEG) at room temperature. The solution was heated to 170 ℃, and then $SnCl_2$ (1.3 g in 10 mL of TEG) was added. A freshly prepared solution of $NaBH_4$ (2.64 g in 50 mL of TEG) was then added dropwise while stirring. After 10 min at 170 ℃, iron (0.74g $FeCl_36H_2O$ in 30 ml of TEG) and cobalt ions (0.5 g $CoCl_26H_2O$ in 30 ml of TEG) solutions were sequentially added. The solution was then heated to 190 ℃ with continued stirring. After alloying for 2 h, a color evolution from gray to black can be observed. The preparation was carried out under flowing argon to avoid the oxidation of the ions. The resulting powders were separated from the solvent by centrifugation, washed with ethanol and dried under vacuum at 80℃. The same approach was used for Sn_2Fe, except that there is no need to join cobalt ions solution.

Material characterization

The morphologies and structures of the as-prepared intermetallic SnFeCo nano particles were characterized by field emission scanning electron microcopy (LEO 1530, HITACHI S-4800) and high resolution transmission electron microcopy (HRTEM, JEM-2100). Power X-ray diffraction (XRD, Philips X'pert Pro Super X-ray diffract meter, Cu Kα radiation) was used for phase analysis. Inductively Coupled Plasma Atomic Emission Spectrometer (ICP-AES, BIRAD PS-4, 1.1 kw, 27 MHz) was used for the exact element content analysis. The X-ray photoelectron spectroscopy (XPS) analysis was performed with a QUANTUM 2000 spectrometer using a focused monochromatized Al Kα radiation (1486.6 eV). The pass energy was 60 eV for the survey spectra and 20 eV for particular elements.

Electrochemical measurements:

The electrochemical performances of as-prepared intermetallic SnFeCo nanocrystals were characterized by assemble them into coin cells (type CR2025) in an argon-filled glove box under conditions that the content of moisture and oxygen were both below 1 ppm. The anode was prepared by spreading a mixture of 80 wt % intermetallic SnFeCo powder, 10 wt % acetylene black and 10 wt % LA133 binder onto a copper foil current collector. The as-prepared electrodes were dried at 80 ℃ in a vacuum oven for 12 h. The anode was separated from lithium by a separator (Celgard 2400). The electrolyte was made from $LiPF_6$ (1M) in a mixture of ethylene carbonate (EC)/ dimethyl carbonate (DMC)/ diethyl carbonate (DEC) in a volume ratio of 1:1:1 with 2 wt % vinylene carbonate (VC) as additive. The cells were galvanostatically charged and discharged in a battery test system (LAND-V34, Land Electronic Co., Ltd., Wuhan) at a current density of 50 mA g^{-1} for a cut-off voltage of 0.02-1.5 V (vs. Li/Li^+) at room temperature.

Calculation procedure:

All the calculations reported herein were performed based on density functional theory (DFT) as implemented in the Vienna Ab-initio Simulation Package (VASP)[20,21]. The electronic exchange correlation energy was modeled using the Perdew–Burke– Ernzerhof (PBE) function within the generalized gradient approx- imation (GGA)[22]. The wave functions were expanded in plan-wave basis up to a kinetic energy cut-off of 350 eV. Brillouin-zone integrations were performed by using special k-point sampling of the Monkhorst–Pack scheme [23] with a 5×5×6 grid. The atomic positions and cell parameters are fully relaxed until the Hellmann–Feynman forces on all the atoms are smaller than 0.01 eV/ Å.

Results and discussion

Figure 1 shows the XRD pattern of SnFeCo alloy. The pure Sn_2Fe phase (JCPDS No: 00-004-0745) can be found in the XRD pattern, whose peaks at 33.63°, 35.01°, 38.99°, 43.81°, 56.35°, 61.06°, 67.21° and 70.61° corresponding to the diffraction peaks of (002), (211), (122), (202), (002), (213), (402) and (004) crystal facets. There are no peaks of SnCo alloy and impurities in this pattern, which may be due to the low quantity of cobalt. All the peaks are very sharp, indicating the alloy structure is well crystallized.

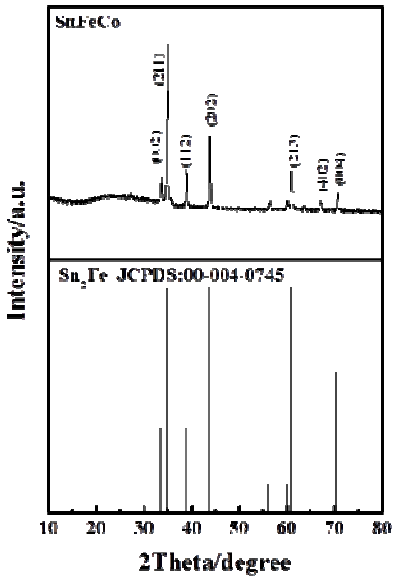

Fig. 1 XRD pattern of the SnFeCo alloy composite.

In order to further verify the composition of the material, ICP-AES was used for analysis and the results are listed in Table 1 as followed. As shown in the table, the output ratio is lower than the input ratio for cobalt. This is probably because the excessive cobalt lost in the centrifugal cleaning process and the other part form SnCo alloy with tin element. In accordance with the element ratio, the theoretical capacity can be calculated as 781 mAh·g^{-1}.

Table 1 The mol ratio of elements of SnFeCo alloy composites.

Element	Input ratio	Output ratio
Fe	1.00	1.00
Co	0.20	0.14
Sn	2.00	2.00

The textural properties were characterized by scanning electron microscopy (SEM) as shown in Figure 2 (a). From the Figure 2, we can see the SnFeCo alloy particle is in cubic-like morphology due to the body-centered tetragonal structure. And the distribution of the grain-size of particles was presented in Figure 2(b), as shown in the figure the average particle size is about 106 nm with narrow distribution.

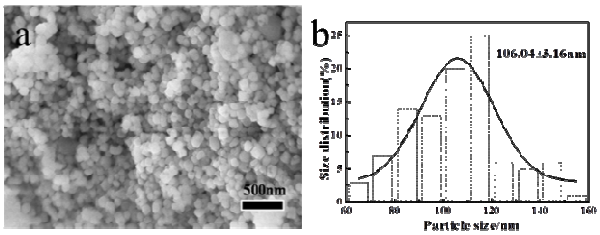

Fig. 2 (a) SEM image of SnFeCo alloy composite (b) Distribution of the grain-size of SnFeCo alloy composite.

The dark-field diffraction in Figure 3(a) shows that one big particle is composited of various surface with different brightness. The corresponding SAED patterns of Figure 3(a) marked with "1" and "2" are respectively presented in Figure 3(b) and Figure 3(c). The SAED pattern in Figure 3(b) shows a single crystal structure that can be indexed to the (211) plane of Sn_2Fe (2.58 Å) , consistent with the XRD results. However, the SAED pattern in Figure 3(c) can be indexed to two kinds of single crystal planes. The spots marked with "△" could be indexed to the (211) plane of Sn_2Fe (2.58 Å, JCPDS: 00-004-0745), and the spots marked with "○" could be indexed to the (211) plane of Sn_2Co (2.51 Å, JCPDS: 03-065-5843).

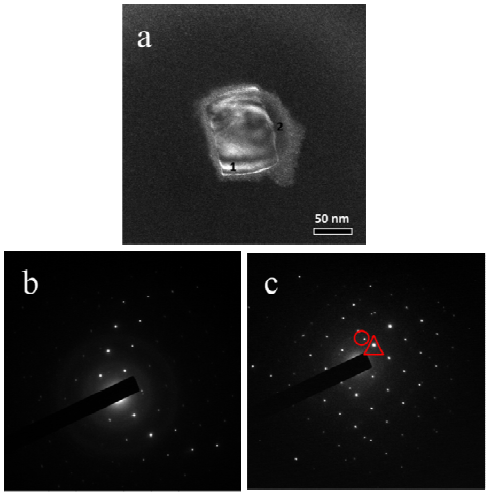

Fig. 3 TEM images of SnFeCo alloy composite (a) Dark-field diffraction of SnFeCo alloy composite (b) The corresponding SAED patterns of SnFeCo alloy composite from the selected area marked with "△"(c) The corresponding SAED patterns of SnFeCo alloy composite from the selected area marked with "○".

The TEM images in Figure 4 are further evidence that the as-prepared alloy is a biphase mixture. From the HR-TEM image (Fig. 4(b)), we can see there are two crystal planes combine together with an angle of 49.1°. And the two lattice fringes with the lattice spacing of 2.71 Å and 2.58 Å, matching fairly well with (002) plane for Sn_2Co and (211) plane for Sn_2Fe.

To identify the assignment of the element in the alloy mixture, EDX spectra are obtained from the respective areas in Figure 5(a) and the atomic ratios are displayed in Table 2. The TEM image in Figure 5(a) reveals that one big particle is always arranged by some small grains with obvious grain boundary. And the element distribution in Table 2 indicates that the low quantity of cobalt is evenly distributed.

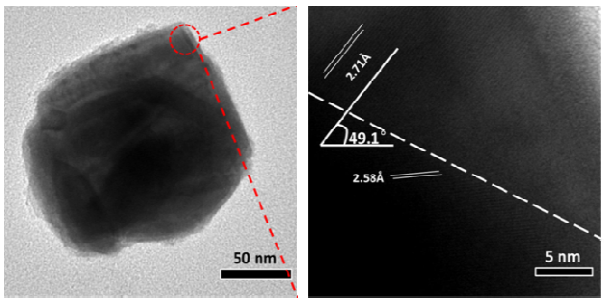

Fig. 4 (a) TEM image of one single SnFeCo alloy particle (b) The corresponding HR-TEM image from the selected area.

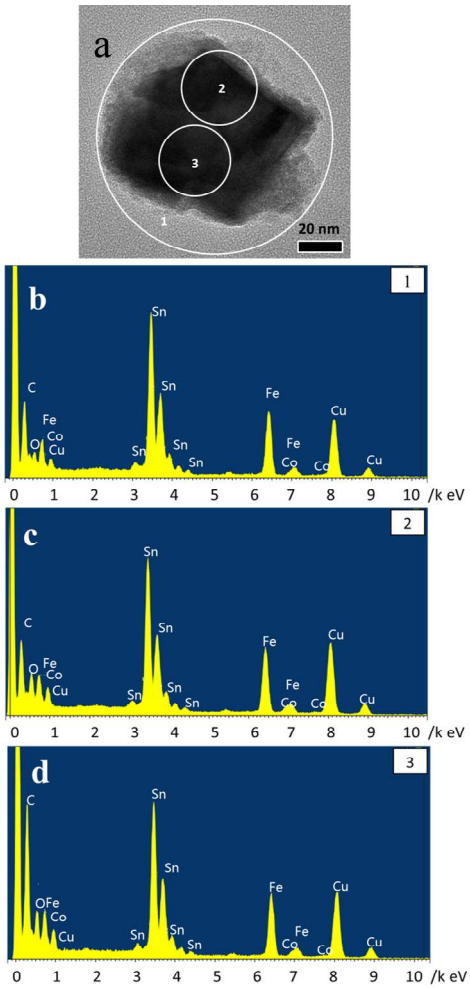

Fig. 5 (a) TEM image of one single SnFeCo alloy particle (b) The corresponding EDX image from the selected area 1 in (a), (c) The corresponding EDX image from the selected area 2 in (a), (d) The corresponding EDX image from the selected area 3 in (a).

Table 2 The distribution of the element in Figure 5.

Element	Area 1	Area 2	Area 3
Fe	16.46%	17.41%	12.40%
Co	1.38%	0.86%	0.97%
Sn	24.46%	27.68%	19.63%

In consideration of the data above, we can confirm that the composite material is composited of two kinds of alloy Sn_2Fe and Sn_2Co. And based on the existing data we can make speculation as follow: assume that all Co formed Sn_2Co alloy with Sn (due to Sn_2Co has lower Gibbs Energy and better chemical stability than Sn_2Fe as shown in Table 3 in the following section) and small part of Fe formed iron oxides due to the higher oxidation activity compared with Sn and Co (some lattice fringes attributed to Fe_2O_3 are found in HR-TEM diffraction patterns Fig. S1). According to the speculation, we can calculate the ratio of these two alloys: Sn_2Fe: Sn_2Co = 0.86: 0.14.

To make the whole reaction process more clearly and straightforward, we have proposed a possible growth mechanism of the SnFeCo alloy composite based on the above discussion (as shown in Figure 6). Firstly, Sn^{2+} was reduced to Sn by $NaBH_4$ coated with PVP. In the second step, subsequently dropping of Fe^{3+} and Co^{2+} adsorbed on the surface of the Sn particles through the PVP molecules and reduced to Fe and Co under the effect of $NaBH_4$. Finally, the inter-diffusion process of these metal occurred at a relatively high temperature, which formed Sn_2Fe and Sn_2Co with the ratio of Sn_2Fe: Sn_2Co = 0.86: 0.14.

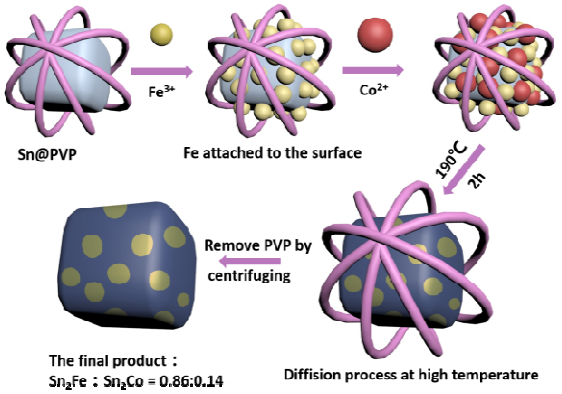

Fig. 6 Schematic illustration of the formation mechanism of SnFeCo alloy composites.

Figure 7(a) presents the data in terms of cycling performance of the SnFeCo alloy composite electrode and Sn_2Fe alloy electrode at a current density of 50 mAh g^{-1}. The first discharge capacity is 828 mAh g^{-1} and the initial coulomb efficiency is 71%. After 50 cycles, the reversible discharge capacity slightly decreases from 585 mAh g^{-1} to 507 mAh g^{-1} with high retention of 87% of that in the second cycle. Compared with SnFeCo alloy, the Sn_2Fe alloy electrode has shown a poorer cycling performance. The first discharge capacity is 799 mAh·g^{-1} and the initial coulomb efficiency was 68%. After 30 cycles, the reversible discharge capacity rapidly decreases from 541 mAh g^{-1} to 0 mAh g^{-1}. The rate capacity of the SnCoFe composite electrode is demonstrated in Figure 7(b), which illustrates stable cyclic response at progressively increasing rates. Even with the current density of 1000 mAh g^{-1}, the electrode can still deliver about 443 mAh g^{-1}, demonstrating that the biphase mixture composite exhibit good electrochemical performance.

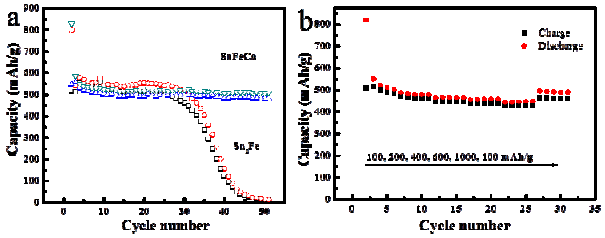

Fig. 7 (a) Cycle performances of the SnFeCo alloy composite and Sn2Fe alloy electrodes (b)Rate performance of of the SnFeCo alloy composite.

The SnFeCo alloy composite electrode charge/discharge performance of 1st, 2nd, 10th and 50th cycles is illustrated in Figure 8(a). The extra discharge capacity in the first cycle may be attributed to the side reaction on the nanomaterial surface. The first discharge capacity fade may be caused by the irreversible lithium loss due to the formation of a solid electrolyte (SEI) layer [24] .The first discharge step produced a long slop voltage plateau at 1.5-0.02 V, which is associated with the intercalation of oxides or the decomposition of electrolyte. The followed voltage plateau at around 0.5 V, exhibiting a typical trend for tin-based electrode, attributes to the alloying reaction as follow [25]:

$$Sn_2Fe+8.8Li^++8.8e^-\rightarrow 2Li_{4.4}Sn+Fe \quad (1)$$
$$Li_{4.4}Sn\leftrightarrow Sn+4.4\ Li^++4.4\ e^- \quad (2)$$
$$Sn_2Co+8.8Li^++8.8e^-\rightarrow 2Li_{4.4}Sn+Co \quad (3)$$
$$Li_{4.4}Sn\leftrightarrow Sn+4.4\ Li^++4.4\ e^- \quad (4)$$

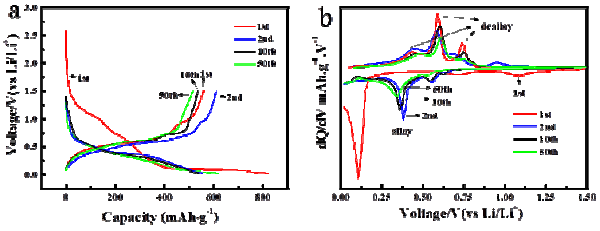

Fig. 8 (a) Charge/discharge curves of the SnFeCo alloy composite electrode (b) Differential capacity curves of the SnFeCo alloy electrode.

To understand the electrochemical behaviours in the 1st, 2nd, 10th and 50th cycle differential capacity curves are recorded and are compared in Figure 8(b).In the first cycle, there are three irreversible reduction peaks at 0.11 V, 0.71 V and 1.07 V. The first peak is generally attributed to the irreversible reaction (1) as above [26] and disappears in the subsequent cycles, which indicates that the reversible reaction (2) will become the dominant reaction after initial cycle [27] . The other peaks may be corresponding to the reduction of tin oxides or the formation of a solid electrolyte interphase (SEI) layer [28-29]. In the subsequent cycles, reduction peaks around 0.3 V and 0.56 V

attribute to the formation of Li-Sn alloy [30-32] . The peak weakens after 50th cycle, which indicates the decline of volume expansion [19, 33]. During the discharge process, three peaks around 0.45 V, 0.59 V and 0.75 V corresponding to the dealloy process of Li_xSn [28]. The dealloying peak around 0.75 V represents the agglomeration of Sn atoms [34]. In this work, we prepared tin-based alloy to avoid this process. As a result, there is a weak peak around 0.75 V with decay in subsequent cycles, which indicates the electrode material has a good cycling performance without obvious agglomeration.

In consideration of the relationship between the crystal structure change and the mechanism of electrochemical reaction, we have used the Vienna Ab-initio Simulation Package (VASP) to calculate crystal structure parameters of the as-prepared alloy .The simulation results are shown in Table 3, and the schematic diagram about the mechanism of electrochemical reaction is displayed in Figure 9 (In Figure 9, the gray balls represent as tin, the blue balls represent as copper, the yellow balls represent as iron and the green balls represent as lithium). It's worth noting that Sn_2Fe and Sn_2Co have the similar crystal structure: (1) the space groups are both tetragonal, (2) have the similar lattice parameters (Sn_2Fe: a = b = 6.38 Å c = 5.46 Å, Sn_2Co: a = b = 6.37 Å c = 5.46 Å), (3) have the similar cell volume (Sn_2Fe: 222.41 $Å^3$, Sn_2Co: 221.88 $Å^3$). These results can be another proof that the two kinds of alloys can be mixed uniformly by facile thermal diffusion alloying reaction.

Table 3 The crystal structure simulation results of Sn_2Fe, Sn_2Co, Fe and Co through VASP method.

	Lattice Parameter Å	Space group	Cell Volume $Å^3$	Gibbs Energy KJ/mol
Sn_2Fe	a = b = 6.38 c = 5.46	I4/mcm (tetragonal)	222.41	$1.516 \cdot 10^3$
Sn_2Co	a = b = 6.37 c = 5.46	I4/mcm (tetragonal)	221.88	$1.444 \cdot 10^3$
Fe	a = b = c = 2.75	Im-3m(fcc)	20.90	$0.757 \cdot 10^3$
Co	a = b = c= 3.45	Fm3m(fcc)	41.23	$0.425 \cdot 10^3$

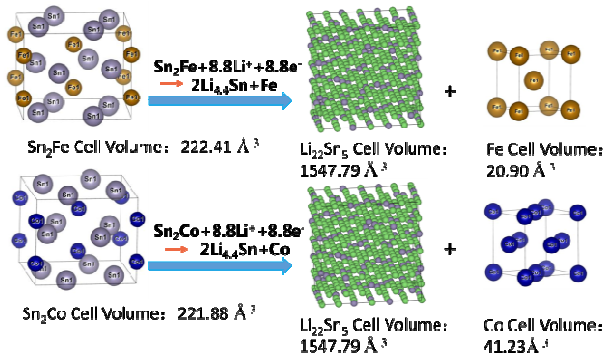

Fig. 9 The brief schematic diagram about the electrochemical mechanism of Sn_2Fe and Sn_2Co composite.

Consider all the data above, the mechanism of electrochemical reaction of the alloy composite can be summarized as shown in Figure 9. In the discharging process, the composite is alloying to be $Li_{4.4}Sn$ and relevant metallic material, the volume expands several times. And it dealloys to be tin with shrink in volume after charging process. The inactive phase M (M = Fe, Co) offers buffer matrix to relief volume expansion during the charge–discharge process and also plays a role in maintaining the integrity between the particles, the active material and the current collector.

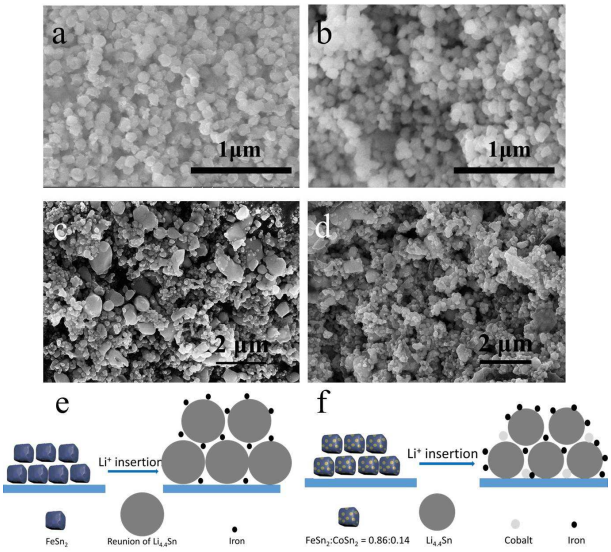

Fig. 10 (a) the SEM image of the prepared $FeSn_2$ (b) the SEM image of the prepared SnFeCo alloy (c) the SEM image of the $FeSn_2$ electrode after 20 cycles (d) the SEM image of the SnFeCo alloy electrode after 20 cycles (e, f) Model of the process of lithium insertion and removal for $FeSn_2$ and SnFeCo electrodes.

In order to illuminate the superiority of the bi-phase mixture of tin-based alloy further, we have analyzed the post-cycling microstructure characterization. As shown in Figure 10, we can see the particle reunion tends to easily happen in the single-phase (due to the soft texture and active surfaces of $Li_{4.4}Sn$ and Sn), which lead to the not uniform particle size distribution. While the agglomeration can be weakened to a large extent in multiphase because there are more phase boundary on the surface. It's well known that the uniform nano-particles can accommodate partly the volume change and also keep the integrity of the active material and matrix, resulting in good cycle performance of the composite electrode.

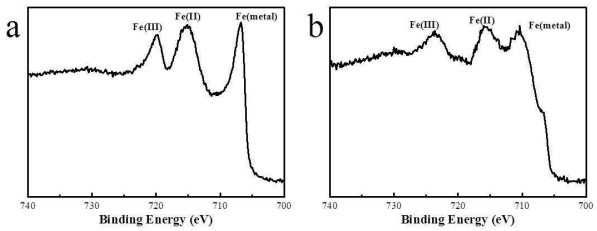

Fig. 10 The XPS spectrum of Fe 2p of (a) the $FeSn_2$ and (b) the SnFeCo placed in the air for a week.

As the XPS spectrum shown in Fig. 11, we can see the Fe in single-phase is more easily oxidized. It may be due to the existence of more stable $CoSn_2$, which can reduce the exposed surface of $FeSn_2$ to some degree, resulting in high stability. Thus the coulomb efficiency can be improved in multi-phase and the good cycle performance can be obtained as a result.

Base on the consideration above, it's easy to visually comprehend the effect of adding cobalt element to $FeSn_2$: (1) $FeSn_2$ and $CoSn_2$ can be equally distributed in the composite alloy because of their similar crystal structure, which can ensure the uniform and stable chemical properties. (2) After

discharging these two alloys can be transform to $Li_{4.4}Sn$ and inactive pure metal M (M = Fe, Co) with equal distribution. The multiphase inactive metallic material with different density can buffer the dimensional change during charge/discharge process effectively. (3) These multiphase inactive metallic material can also play an important role on keeping the integrity between the active material and current collector, preventing the pulverization at the same time. (4) The agglomeration can be weakened to a large extent in multiphase because there are more phase boundary on the surface. It's well known that the uniform nano-particles can accommodate partly the volume change and also keep the integrity of the active material and matrix, resulting in good cycle performance of the composite electrode. (5) The existence of more stable $CoSn_2$ can reduce the exposed surface of $FeSn_2$ to some degree, resulting in high stability. Thus the coulomb efficiency can be improved in multi-phase and the good cycle performance can be obtained as a result.

Conclusions

In summary, the obtained uniform biphase mixture alloy composite was prepared by facile reduction-thermal diffusion reaction. The TEM images show it's composed of Sn_2Fe and Sn_2Co. The Ab-initio Simulation results indicated the Sn_2Fe and Sn_2Co have the similar crystal structure, demonstrating the two kinds of alloys can be mixed uniformly by thermal diffusion alloying reaction. When used as the anode materials, there is a significant improvement of cycling performance for the alloy composite. This may due to the inactive phase M (M = Fe, Co) offers buffer matrix to relief volume expansion during the charge–discharge process and also plays a role in maintaining the integrity between the particles, the active material and the current collector. Therefore, the synthesis of multicomponent alloys to obtain stable, homogeneous nanomaterial is an effective means to improve the cycling performance of tin-based anode materials.

Acknowledgements

This work was supported by the NSFC (Grant Nos. 21273184 and 21321062), the "973" program (Grant No. 2015CB251102) and SRFDP (20130121110002).

Notes and references

[a] Department of Chemistry, College of Chemistry and Chemical Engineering, State Key Laboratory of Physical Chemistry of Solid Surfaces, Xiamen University, Xiamen, 361005, China.
[b] College of Energy Research, Xiamen University, Xiamen, 361005, China.
E-mail: huangl@xmu.edu.cn

† Electronic Supplementary Information (ESI) available: **Figure S1** (a) TEM image of one single SnFeCo alloy particle (b) The corresponding HR-TEM image from the selected area.

1 J. S. Chen, Chang Ming Li, W. W. Zhou, Q. Y. Yan, L. A. Archer, X. W. Lou, *Nanoscale*, 2009, 1, 280-285.
2 Q. Wang, Q. Wang, D. A. Zhang, J. Sun, L. L. Xing, X. Y. Xue, *Chem. Asian J*., 2014, 9, 3299-3306.
3 Q. Wang, D. A. Zhang, Q. Wang, J. Sun, L. L. Xing, X. Y. Xue, *Electrochim. Acta*, 2014, 46, 411-418.
4 B. Liu, A. Abouimrane, D. E. Brown, X. F. Zhang, Y. Ren, Z. Z. Fang, K. Amine, *J. Mater. Chem. A*, 2013, 1, 4376-4382.
5 L. G. Xue, X. Xia, T. Tucker, K. Fu, S. Zhang, S. L. Li, X. W. Zhang *J. Mater. Chem. A*, 2013, 1, 13807-13813.
6 J. Choi, S. Y. Han, J. Jin, J. Kim, J. H. Park, S. M. Lee, H. J. Kim, S U. Son, *J. Mater. Chem. A,* 2013,**1**, 8609-8615.
7 W. Ni, J. L. Cheng, L. Y. Shi, X. D. Li, B. Wang, Q. Guan, L. Huang, G. F. Gu, H. Li, *J. Mater. Chem. A,* 2014, **2**, 19122-19130.
8 T. Brousse , R. Retoux , U. Herterich , D. M. Schleich, *J. Electrochem. Soc*, 1998, **1**, 1-4.
9 M. Winter, I. O. Besenhard, M. E. Spahr, N. Petr, *Adv. Mater*, 1998, **10**, 725-763.
10 J. O. Besenhard, J. Yang, M. Winter, *J. Power Sources*, 1997, **68(1)** ,87-90.
11 K. D. Kepler, J. T. Vaughey, M. M. Thackray, *Electrochemistry Commuication*, 1999, **1**, 111-115.
12 S. F. Fan, L. Y. Lim, Y. Y. Tay, S. S. Pramana, X. H. Rui, M. K. Samani, Q. Y. Yan, B. K. Tay, Michael F. Toney , H. H. Hng, *J. Mater. Chem. A,* 2013, **1**, 14577-14585
13 J. Yang, M. Wachtler, M. Winter, J. O. Besenhard, *Electrochem Solid-state Lett*, 1999, **2(4)**, 161-168.
14 L. Huang, J. S. Cai, Y. He, F. S. Ke, S. G. Sun, *Electrochemistry Communications*, 2009, **11(5)**, 950-953.
15 H. Guo, H. L. Zhao, X. D. Jia X D, J. C. He, W. H. Qiu, X. Li, *J. Power Sources*, 2007, **174**, 921-926.
16 X. L. Wang, W. Q. Han, J. J. Chen, J. Graetz, *ACS Appl Mater Inter*, 2010, **2(5)**, 1548-1551.
17 X. L. Wang, M. Feygenson, H. Chen, C. H. Lin, W. Ku, J. M. Bai, M. C. Aronson, T. A. Tyson, W. Q. Han, *J. Am Chem Soc*. 2011, **133(29)**, 11213-11219.
18 C. Q. Zhang, J. P. Tu, X. H. Huang, *J. Alloy Compd*, 2008, **457**, 81-85.
19 M. Chamas, P. E. Lippens, J. C. Jumas, Y. F. Yuan, S. F. Wang, *J. Power Sources*, 2011, **196**, 7011-7015.
20 G. Kresse, J. Furthmüller, *Computer Mater Soc*. 1996, **6**, 15-50.
21 G. Kresse, J. Furthmüller, *Phys Rev B*. 1996, **54**, 11169-11186.
22 J. P. Perdew, K. Burke, M. Ernzerhof, *Phys Rev Lett*. 1996, **77**, 3865-3868.
23 H. J. Monkhorst, J. D. Pack, *Phys Review B*. 1976, **13**, 5188.
24 U. G. Nwokeke, R. Alcantara, J. L. Tirado, R. Stoyanova, M. Yoncheva, E. Zhecheva, *Chem Mater*, 2010, **22**, 2268-2275.
25 U. G. Nwokeke, R. Alcantara, J. L. Tirado, R. Stoyanovab, E. Zhecheva, *J. Power Sources*, 2011, **196**, 6768-6771.
26 O. Mao, R. D. Dunlap, J. R. Dahn, *J. Electrochem Soc*, 1999, **146**. 405-413.
27 U. G. Nwokeke, R. Alcantara, *J. Alloy Compd*, 2011, **509**, 3074-3079.
28 K. Ui, S. Kikuchi, Y. Jimba, *J. Power Sources*, 2011, **196**, 3916-3920.
29 K. Ui, S. Kikuchi, Y. N. Jimba, S. Kumagaia, S. Ito, *J. Power Sources*, 2009, **189**, 224-229.

30 T. Huang, Y. Yao, Z. Wei, *Electrochimica Acta*, 2010, **56**, 476-482.
31 R. Z. Hu, M. Q. Zeng, M. Zhu, *Electrochimica Acta*, 2009, **54**, 2843-2850.
32 N. Tamura, Y. Kato, A. Mikami, M. Kamino, S. Fujitani, M. Kamino, I. Yonezu, *J. Electrochem Soc*, 2006, **153A**, 1626-1632.
33 U. G. Nwokeke, F. Nacimiento, R. Alcantara, J. L. Tirado, *Electrochem Solid State Lett*, 2011, **14(10)**, 148-150.
34 I. A. Courtney, J. R. Dahn, *J. Electrochem Soc*, 1997, **144(6)**, 2045-2052.